

# Modelling the energy distribution in CHIME/FRB Catalog-1

Siddhartha Bhattacharyya<sup>1</sup>\*, Somnath Bharadwaj<sup>1</sup>, Himanshu Tiwari<sup>2</sup> and Suman Majumdar<sup>3,4</sup>

<sup>1</sup>*Department of Physics, Indian Institute of Technology, Kharagpur, India*

<sup>2</sup>*International Centre for Radio Astronomy Research, Curtin University, Bentley, WA 6102, Australia*

<sup>3</sup>*Department of Astronomy, Astrophysics and Space Engineering, Indian Institute of Technology, Indore, India*

<sup>4</sup>*Department of Physics, Blackett Laboratory, Imperial College, London SW7 2AZ, U.K.*

28 September 2022

## ABSTRACT

We characterize the intrinsic properties of any FRB using its redshift  $z$ , spectral index  $\alpha$  and energy  $E_{33}$  in units of  $10^{33}$  J emitted across 2128 – 2848 MHz in the FRB’s rest frame. Provided that  $z$  is inferred from the measured extra-galactic dispersion measure  $DM_{\text{Ex}}$ , the fluence  $F$  of the observed event defines a track in  $(\alpha, E_{33})$  space which we refer to as the ‘energy track’. Here we consider the energy tracks for a sample of 254 non-repeating low dispersion measure FRBs from the CHIME/FRB Catalog-1, and use these to determine  $n(E_{33} | \alpha)$  the conditional energy distribution i.e. the number of FRBs in the interval  $\Delta E_{33}$  given a value of  $\alpha$ . Considering  $-10 \leq \alpha \leq 10$ , we find that the entire energy scale shifts to higher energy values as  $\alpha$  is increased. For all values of  $\alpha$ , we can identify two distinct energy ranges indicating that there are possibly two distinct FRB populations. At high energies, the distribution is well fitted by a modified Schechter function whose slope and characteristic energy both increase with  $\alpha$ . At low energies, the number of FRBs are in excess of the predictions of the modified Schechter function indicating that we may have a distinctly different population of low-energy FRBs. We have checked that our main findings are reasonably robust to the assumptions regarding the Galactic Halo and Host galaxy contributions to the dispersion measure.

**Key words:** transients: fast radio bursts.

## 1 INTRODUCTION

Fast Radio Bursts (FRBs) are short duration ( $\sim$  ms), high energetic ( $\sim 10^{32} - 10^{36}$  J) dispersed radio pulses first detected at Parkes telescope (Lorimer et al. 2007). Till now, more than 800 FRBs have been reported. The online catalog of these reported event can be found here<sup>1</sup>. These reported FRBs can apparently be divided into two distinct classes (1) repeating FRBs and (2) non-repeating FRBs.

The first repeating FRB event (FRB121102) was reported by Arecibo radio telescope (Spitler et al. 2014), and to-date there has been more than 30 repeating bursts are reported from the same source (FRB121102) with identical values of its dispersion measure ( $DM$ ). Other than Arecibo’s detection, CHIME (Rafiei-Ravandi et al. 2021) and VLA (Law et al. 2020) have also reported the detection of repeating FRBs.

On the other hand, a significant number of non-repeating FRBs  $> 600$  have been reported at various instrument such as CHIME (Rafiei-Ravandi et al. 2021), Parkes (Price et al. 2018), ASKAP (Bhandari et al. 2020), UTMOST (Gupta et al. 2020), FAST (Zhu et al. 2020), GBT (Parent et al. 2020), VLA (Law et al. 2020), DSA-10 (Ravi et al. 2019), Effelsberg (Marcote et al. 2020), SRT (Pilia et al. 2020), Apertif (van Leeuwen et al. 2022), MeerKAT (Rajwade et al. 2022), etc. It is not clear whether the repeating and non-repeating FRBs are events drawn from the same parent population or not. Given the currently available data and the present understanding of FRBs, it is

quite possible that the non-repeating FRBs form a separate population distinct from the repeating FRBs (Caleb et al. 2018; Palaniswamy et al. 2018; Lu & Piro 2019). The work reported here is entirely restricted to the non-repeating FRBs.

Several models have been proposed for the physical origin of the FRB emission. The reader is referred to Zhang (2020) and Platts et al. (2019) for a quick review on the proposed FRB progenitor models. Considering observations, the intrinsic properties of the FRBs like the spectral index  $\alpha$  and the energy distribution are rather poorly constrained. Macquart et al. (2019) have analysed a sample of 23 FRBs detected at ASKAP to infer a mean value of  $\alpha = -1.5^{+0.2}_{-0.3}$ , whereas Houben et al. (2019) have utilised the fact that FRB 121102 was not simultaneously detected at 1.4 GHz and 150 MHz to proposed a lower limit  $\alpha > -1.2 \pm -0.4$ . James et al. (2021) have modelled the FRB energy distribution using a simple power law, and James et al. (2022) have used the FRBs detected at Parkes and ASKAP to constrain the exponent for the energy distribution to a value  $-1.6^{+0.11}_{-0.12}$ . Various studies (Macquart et al. 2019; Houben et al. 2019; James et al. 2021) have each considered a specific telescope for which they have estimated the spectral index  $\alpha$  of the FRB emission.

An earlier work Bera et al. (2016) has modelled the FRB population, and used this to make predictions for FRB detection for different telescopes. In a subsequent work Bhattacharyya & Bharadwaj (2021) have used the two-dimensional Kolmogorov-Smirnov (KS) test to compare the FRBs observed at Parkes, ASKAP, CHIME and UTMOST with simulated predictions for different FRB population models. The parameter range  $\alpha > 4$  and  $\bar{E}_{33} > 60$  was found to be ruled out with 95% confidence, here  $\bar{E}_{33}$  is the mean energy of the

\* sid.phy.in@gmail.com

<sup>1</sup> <https://www.wis-tns.org/>

FRBs population in units of  $10^{33}$  J across 2128 – 2848 MHz in the FRB rest frame. In a recent work (Bhattacharyya et al. 2022) we have used a sample of 82 non-repeating FRBs detected at Parkes, ASKAP, CHIME and UTMOST to perform a maximum likelihood analysis to determine the FRB population model parameters which best fits this data. We have obtained the best fit parameter values  $\alpha = -1.53^{+0.29}_{-0.19}$ ,  $\bar{E}_{33} = 1.55^{+0.26}_{-0.22}$  and  $\gamma = 0.77 \pm 0.24$ , where  $\gamma$  is the exponent of the Schechter function energy distribution of the FRBs.

The CHIME telescope<sup>2</sup> has recently released the CHIME/FRB catalog 1 (Amiri et al. 2021) which has reported the detection of 535 FRBs from 492 different sources among which 462 FRBs are apparently non-repeating. Several studies (Amiri et al. 2021; Rafiei-Ravandi et al. 2021; Chawla et al. 2022; Pleunis et al. 2021; Josephy et al. 2021) have shown that there are at least two distinct classes of FRBs in this catalog, *viz.* (1) where the observed  $DM$  values lie within the range  $100 - 500 \text{ pc cm}^{-3}$  and (2) where the observed  $DM$  values are greater than  $500 \text{ pc cm}^{-3}$ . It has been proposed (Cui et al. 2022) that the low  $DM$  and high  $DM$  FRBs may originate from two different kinds of sources, or the sources may be the same with different environmental conditions accounting for the large  $DM$  values. In the present work we have analyzed the energy distribution of the non-repeating low  $DM$  FRBs in the CHIME/FRB catalog 1. A brief outline of this paper follows. Section 2 presents the methodology, while the results are presented in Section 3 and we present our conclusions in Section 4. In Appendix A we have analyzed how much our results vary if we change the values of  $DM_{\text{Halo}}$  and  $DM_{\text{Host}}$ .

## 2 METHODOLOGY

An observed FRB is characterized by its dispersion measure  $DM$ , fluence  $F$  and pulse width  $w$ . For our analysis we consider 254 non-repeating FRBs detected at CHIME (Amiri et al. 2021) for which the extragalactic contribution to dispersion measure ( $DM_{\text{Ex}}$ ) lie within the range  $50 - 500 \text{ pc cm}^{-3}$ . The  $DM_{\text{Ex}}$  for each FRB is estimated using the equation

$$DM_{\text{Ex}} = DM_{\text{obs}} - DM_{\text{MW}} - DM_{\text{Halo}} \quad (1)$$

where,  $DM_{\text{obs}}$  is the observed dispersion measure and  $DM_{\text{MW}}$  is the Milky Way contribution to  $DM_{\text{obs}}$  which is calculated using the NE2001 model (Cordes & Lazio 2003).  $DM_{\text{Halo}}$  is the Galactic halo contribution to  $DM_{\text{obs}}$ , and we assume a fixed value  $DM_{\text{Halo}} = 50 \text{ pc cm}^{-3}$  (Prochaska & Zheng 2019) for all the FRBs considered here. Figure 1 shows the distribution of  $DM_{\text{Ex}}$  and  $F$  of the 254 non-repeating FRBs considered for this analysis. The  $DM_{\text{Ex}}$  and  $F$  values of these FRBs lie within the range  $50.8 - 496.8 \text{ pc cm}^{-3}$  and  $0.4 - 90 \text{ Jy ms}$  respectively. We do not see any noticeable correlation between  $DM_{\text{Ex}}$  and  $F$  for the FRBs considered here. Further, the dispersion of  $F$  values also appears to be independent of  $DM_{\text{Ex}}$ .

There are no independent redshift measurements for the FRBs considered here, and we have used the extragalactic dispersion measure  $DM_{\text{Ex}}$  to infer the redshifts ( $z$ ) and hence the cosmological distances of the FRBs. Considering a homogeneous and completely ionized intergalactic medium (IGM), the  $DM_{\text{Ex}}$  can be modelled as

$$DM_{\text{Ex}}(z) = 940.51 \int_0^z dz' \frac{1+z'}{\sqrt{\Omega_m(1+z')^3 + \Omega_\Lambda}} + \frac{DM_{\text{Host}}}{1+z} \quad (2)$$

where the first term is the contribution from the inter-galactic medium (IGM) and the second term is the contribution from the host galaxy

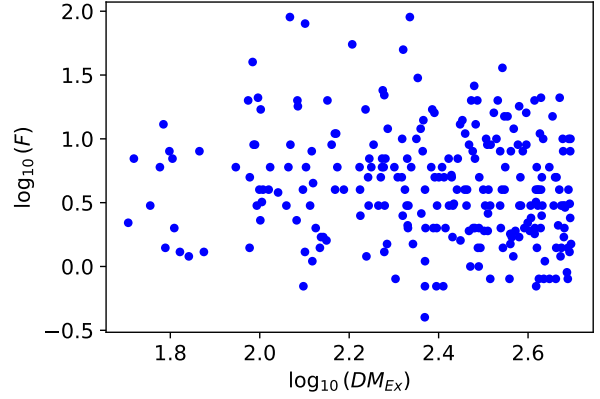


**Figure 1.** The distribution of  $DM_{\text{Ex}}$  the extragalactic dispersion measure and  $F$  the observed fluence of the 254 non-repeating FRBs considered here. Using a fixed value of  $DM_{\text{Host}} = 50 \text{ pc cm}^{-3}$ , the redshift range of these FRBs is  $0.001 \leq z \leq 0.46$ .

of an FRB. The unknown  $DM_{\text{Host}}$  is not well constrained for most of the unlocalized FRBs to date. Further,  $DM_{\text{Host}}$  depends on the intersection of the line of sight to the FRB with the disk of the host galaxy. For the present analysis we mainly consider two scenarios for  $DM_{\text{Host}}$ , (1) a fixed value  $DM_{\text{Host}} = 50 \text{ pc cm}^{-3}$  for all the FRBs and (2) a random value of  $DM_{\text{Host}}$  drawn from a log-normal distribution with mean  $\log(50)$  and variance 0.5. This two scenarios are denoted here as  $DM_{50}$  and  $DM_{\text{Rand}50}$  respectively. In addition to this, we have also repeated the entire analysis for several other choices of  $DM_{\text{Halo}}$  and  $DM_{\text{Host}}$  for which the results are presented in the Appendix.

The aim of this analysis is to model the energy distribution of the sample of 254 FRBs detected at CHIME. The FRB population model used here is presented in Bera et al. (2016), and the reader is referred there for details. We have modelled the intrinsic properties of an FRB using its spectral index  $\alpha$ , energy  $E$  and intrinsic pulse width  $w_i$ . The pulse width does not figure in the present work, and we do not consider this here. We first consider  $E_\nu$  the specific energy of an FRB which is defined as the energy emitted in the frequency interval  $d\nu$  centred at the frequency  $\nu$ . We model this as

$$E_\nu = E \phi(\nu) \quad (3)$$

where  $E$  is the energy emitted in the frequency interval  $\nu_a = 2128 \text{ MHz}$  to  $\nu_b = 2848 \text{ MHz}$  in the rest frame of the source, and  $\phi(\nu)$  is the emission profile which we have modelled as a power law  $\phi(\nu) \propto \nu^\alpha$ . We have assumed that all the FRBs have the same value of the spectral index  $\alpha$ . It is also convenient to introduce the average emission profile  $\bar{\phi}(z, \alpha)$  which refers to a situation where an FRB at redshift  $z$  is observed using a telescope which has a frequency coverage of  $\nu_1$  to  $\nu_2$ . We then have

$$\bar{\phi}(z, \alpha) = \left( \frac{\nu_2^{1+\alpha} - \nu_1^{1+\alpha}}{\nu_1^{1+\alpha} - \nu_2^{1+\alpha}} \right) \frac{(1+z)^\alpha}{\nu_2 - \nu_1} \quad (4)$$

which is the average emission profile at the rest frame of the source. Considering observations with CHIME, we have used  $\nu_1 = 400 \text{ MHz}$  to  $\nu_2 = 800 \text{ MHz}$  for the subsequent analysis.

For an FRB with energy  $E$  and spectral index  $\alpha$  located at redshift  $z$ , the fluence  $F$  of the observed event is predicted to be

$$F = \frac{E \bar{\phi}(z, \alpha) B(\vec{\theta})}{4\pi r^2(z)} \quad (5)$$

where  $B(\vec{\theta})$  is the beam pattern of the telescope at the angular position

<sup>2</sup> <https://www.chime-frb.ca/home>

**Table 1.** The  $DM_{\text{Ex}}$  and  $F$  values of the four specific FRBs detected at CHIME.

FRB	$DM_{\text{Ex}}$ (pc cm <sup>-3</sup> )	$F$ (Jy ms)	Comment
FRB1	50.8	2.2	FRB with minimum $DM_{\text{Ex}}$
FRB2	496.8	1.5	FRB with maximum $DM_{\text{Ex}}$
FRB3	233.9	0.4	FRB with minimum $F$
FRB4	216.6	90.0	FRB with maximum $F$

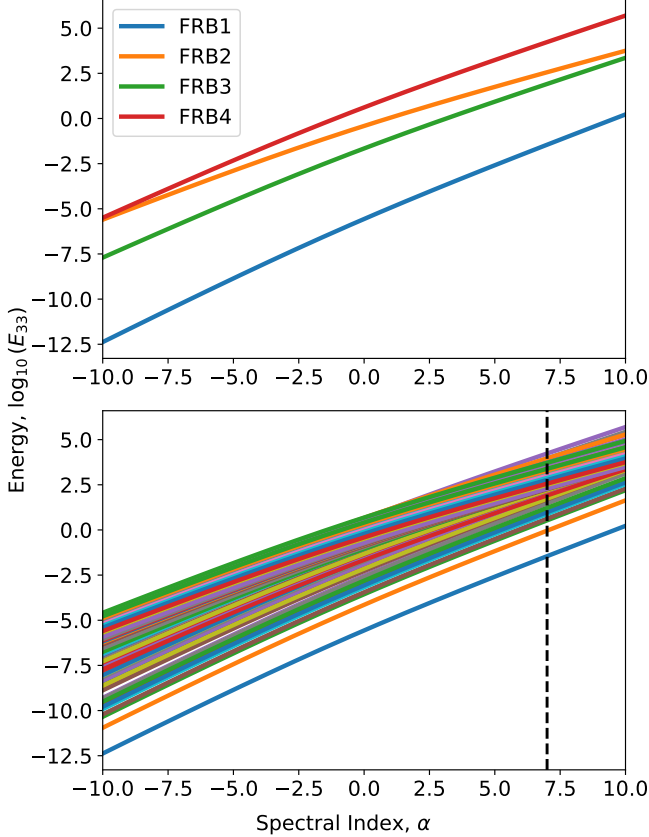


**Figure 2.** The energy tracks i.e. the variation of the intrinsic energy  $E_{33}$  with the spectral index  $\alpha$  for the four specific FRBs (upper panel) and for all 254 FRBs (lower panel) considered for this analysis. The vertical line in the lower panel corresponds to  $\alpha = 7$ .

$\vec{\theta}$  of the event, and  $r(z)$  is the comoving distance to the source which we have estimated using the flat  $\Lambda$ CDM cosmology (Aghanim et al. 2020). The FRBs in our sample have all been detected very close to the beam center ( $|\vec{\theta}| \leq 0.05$ ) for which  $B(\vec{\theta}) \approx 1$  (Amiri et al. 2021), and the redshifts have all been inferred from  $DM_{\text{Ex}}$  using eq. (2). Finally we can use eq. (5) to predict the observed fluence  $F$  for any FRB in our sample provided we know two intrinsic properties of the FRB namely its energy  $E$  and spectral index  $\alpha$ . Conversely, the observed fluence imposes a relation between  $E$  and  $\alpha$  which we can visualise as a track in the  $\alpha - E$  plane. We refer to this as the "energy track" of the FRB. It is further convenient to express the energy in units of  $10^{33}$  J which we denote as  $E_{33}$ .

The upper panel of Figure 2 shows the energy tracks corresponding to four of the extreme FRBs in our sample for which  $DM_{\text{Ex}}$  and  $F$  are tabulated in Table 1. Considering the two observed quantities  $DM_{\text{Ex}}$

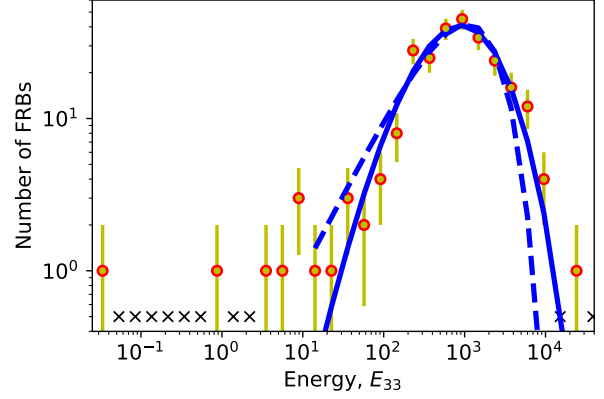


**Figure 3.** The red circles show  $N(E_{33} | \alpha)$  as a function of  $E_{33}$  for  $\alpha = 7$ , and the yellow vertical lines show the  $1\sigma$  Poisson errors. The black cross marks show the position of the empty bins. Considering eq. (7), the blue dashed and solid lines show the predictions for the best fit with  $\beta = 1$  and  $\beta = 0.25$  respectively.

and  $F$ , the shape of the track depends on  $DM_{\text{Ex}}$  (or equivalently  $z$ ) through  $\bar{\phi}(z, \alpha)$  whereas the track just scales up or down if the value of  $F$  is changed. The term  $\bar{\phi}(z, \alpha)$  accounts for the fact that we are actually probing a different frequency range for FRBs at different redshifts. The shape of  $\bar{\phi}(z, \alpha)$  as a function of  $\alpha$  changes with  $z$ . The FRBs in our sample are all in the range  $z < 1$  for which the energy tracks are all found to all have a positive slope. Comparing the tracks for FRB1 and FRB2, which have the highest and lowest  $z$  respectively, we see that the track gets flatter as  $z$  is increased. In fact, the slope reverses at  $z \sim 4$ , however our sample does not extend to such high  $z$ . The FRBs with the minimum and maximum fluence (FRB3 and FRB4 respectively) are also shown. Comparing the four FRB tracks, we see that the track for FRB1 lies considerably below the other three tracks which appear to lie close together within a band. This suggests that FRB1, which is the nearest FRB, is intrinsically much fainter (lower  $E_{33}$ ) compared to the other three FRBs shown in the figure.

The lower panel of Figure 2 shows the energy tracks for all the 254 FRBs considered for the present analysis. We see that most of the FRB tracks are concentrated in a band which runs nearly diagonally across the figure, and the band gets narrow in its vertical extent ( $E_{33}$ ) as  $\alpha$  is increased. The tracks of a few of the faintest FRBs, particularly the nearest one (FRB1 of Table 1), appear to lie distinctly below the band which encompasses the majority of the FRBs.

The analysis presented till now has used the observed  $DM_{\text{Ex}}$  and  $F$  values of our FRB sample to constrain the intrinsic FRB properties to a limited region of the two dimensional  $\alpha - E_{33}$  parameter space as shown in Figure 2. However, for the subsequent analysis we focus on the one dimensional FRB energy ( $E_{33}$ ) distribution. We have modelled this using  $n(E_{33} | \alpha)$  the conditional energy distribution which is defined as the numbers of FRBs in the energy interval  $\Delta E_{33}$  centred around a value  $E_{33}$  given a fixed value of  $\alpha$ . Considering the observational data, it is more convenient to estimate  $N(E_{33} | \alpha)$  which is the number of FRBs in bins of equal logarithmic width  $\Delta(\log_{10} E_{33}) = 0.2$  given a fixed value of  $\alpha$ . The two quantities introduced here are related as

$$N(E_{33} | \alpha) = 0.451 E_{33} \times n(E_{33} | \alpha). \quad (6)$$

The procedure for estimating  $N(E_{33} | \alpha)$  is illustrated in Figure 2 for  $\alpha = 7$  which is indicated by the vertical black dashed line. The  $E_{33}$  distribution along this vertical line is divided into bins of width

$\Delta(\log_{10} E_{33}) = 0.2$  for which  $N(E_{33} | \alpha)$ , the number of FRBs in each bin, is shown in Figure 3. The black crosses mark the bins which do not contain any FRB *i.e.*  $N(E | \alpha) = 0$ , and the  $1 - \sigma$  error-bars correspond to  $\sqrt{N(E | \alpha)}$  the expected Poisson fluctuations.

Considering Figure 3, we see that  $N(E_{33} | \alpha)$  shows two distinctly different behaviour in two different  $E_{33}$  ranges. At low energies in the range  $E_{33} < 10$  we find several  $E_{33}$  bins which have only a few ( $\sim 1 - 3$ ) FRBs each, whereas the remaining low  $E_{33}$  bins do not contain any FRBs at all. We refer to this energy range as 'LELN' - low  $E_{33}$  low  $N(E_{33} | \alpha)$ . We see that we have considerably higher numbers of FRBS in each bin at higher energies in the range  $E_{33} = 10^2 - 10^4$ . We refer to this energy range as 'HEHN' - high  $E_{33}$  high  $N(E_{33} | \alpha)$ .

We now focus on the FRBs in the HEHN range. Here we see that  $N(E_{33} | \alpha)$  exhibits a peak at a characteristic energy  $E_{33} \approx 10^2$ . Further,  $N(E_{33} | \alpha)$  appears to increase relatively gradually with  $E_{33}$  in the range  $E_{33} < E_0$ , and it falls off rapidly (nearly exponentially) for  $E_{33} > E_0$ . We find a similar behaviour also for other value of  $\alpha$  (discussed later). Based on this we have modelled  $n(E_{33} | \alpha)$  in the HEHN range as

$$n(E_{33} | \alpha) = K(\alpha) \left( \frac{E_{33}}{E_0(\alpha)} \right)^{\gamma(\alpha)} \exp \left[ - \left( \frac{E_{33}}{E_0(\alpha)} \right)^{\beta} \right] \quad (7)$$

where  $\gamma(\alpha)$ ,  $E_0(\alpha)$  and  $K(\alpha)$  are three parameters whose values are determined by fitting the observed  $N(E_{33} | \alpha)$  individually for each value of  $\alpha$ . We have not included  $\beta$  as a parameter in the fit. However, we have tried out several discrete values of  $\beta$  in order to assess which provides a good fit over the entire  $\alpha$  range. Considering  $\beta = 1$  we see that eq. (7) corresponds to the Schechter function where  $n(E_{33} | \alpha)$  and  $N(E_{33} | \alpha)$  both decline exponentially for  $E_{33} > E_0$ . Figure 2 shows the results for the best fit Schechter function where we see that for  $E_{33} > E_0$  the predicted  $N(E_{33} | \alpha)$  declines faster than the actual number of observed FRB events. We find that the slower decline predicted for  $\beta = 0.25$  gives a better fit to the observed  $N(E_{33} | \alpha)$ , particularly for  $E_{33} > E_0$ . Eq. 7 with  $\beta = 0.25$  (solid blue line) provides a better fit to the observed data in comparison to  $\beta = 1$  (dashed blue line), where the reduced  $\chi^2$  have values  $\chi_{\text{dof}}^2 = 1.06$  and  $2.72$  for  $\beta = 0.25$  and  $1$  respectively. Here we have identified the first five non-empty low  $E_{33}$  bins as the LELN range which was excluded from the fitting procedure. We refer to eq. 7 with  $\beta = 0.25$  as the "modified Schechter function". Further, in the subsequent discussion we do not explicitly show  $\alpha$  as an argument for the parameters  $K$ ,  $E_0$  and  $\gamma$  for brevity of notation. The methodology outlined here for  $\alpha = 7$ , was used for a range of  $\alpha$  values for which the results are presented below.

### 3 RESULTS

We have estimated  $N(E_{33} | \alpha)$  considering  $\alpha$  in the range  $-10 \geq \alpha \geq 10$ . The different panels of Figure 4 show the results for  $\alpha = -10, -5, -2, 0, 5$  and  $10$  respectively, all considering  $DM_{\text{Host}} = 50 \text{ pc cm}^{-3}$  fixed, and we refer to this as  $DM_{50}$ . We see that the behaviour is very similar for all values of  $\alpha$ , with the difference that the entire energy scale shifts to higher values as  $\alpha$  is increased. In all cases we see that  $N(E_{33} | \alpha)$  shows two distinctly different behaviour in two different energy ranges. For all values of  $\alpha$ , at low  $E_{33}$  we find several  $E_{33}$  bins which have only a few ( $\sim 1 - 3$ ) FRBs each, whereas the remaining low  $E_{33}$  bins are empty. Here we have identified the first five non-empty low  $E_{33}$  bins as the LELN range. At higher  $E_{33}$ , we see that  $N(E_{33} | \alpha)$  initially increases with  $E_{33}$ , reaches a peak value and then declines. We refer to this as the HEHN range.

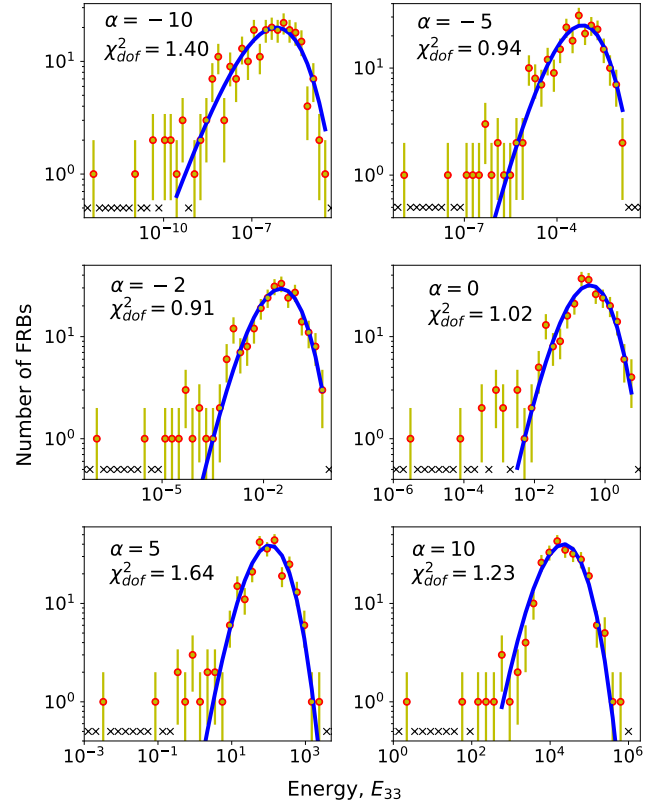


**Figure 4.** Considering  $DM_{50}$ , the red circles show  $N(E_{33} | \alpha)$  as a function of  $E_{33}$  for different values of  $\alpha$  as mentioned in the figure panels, and the yellow vertical lines show the  $1\sigma$  Poisson errors. The black cross marks show the position of the empty bins. Considering eq. (7), the blue solid lines shows the predictions for the best fit modified Schechter function ( $\beta = 0.25$ ) while the corresponding values of the reduced chi-squared  $\chi_{\text{dof}}^2$  are mentioned in the respective figure panels.

The energy distribution in the HEHN regime appears to be distinctly different from that in the LELN regime, and for the subsequent fitting we have excluded the FRBs in the LELN range. The best fit  $N(E_{33} | \alpha)$  (blue line) and the  $\chi_{\text{dof}}^2$  values are shown in the different panels of Figure 4. In all cases we find that the modified Schechter function provides a good fit to  $N(E_{33} | \alpha)$  in the HEHN regime. We also see that in the LELN regime the observed  $N(E_{33} | \alpha)$  values are considerably in excess of the predictions of the modified Schechter function, indicating that the low energy FRBs have an energy distribution which is different from that of the high energy FRBs.

We next consider the variation of  $\gamma$  and  $E_0$  with  $\alpha$  as shown in Figure 5. We first consider the upper panel where the solid blue line shows the variation of  $\gamma$  with  $\alpha$ . We see that  $\gamma$  increases nearly linearly from  $\gamma \approx -0.25$  at  $\alpha = -10$  to a maximum value of  $\gamma \approx 2.43$  at  $\alpha = 6.5$  beyond which it declines slightly to  $\gamma \approx 2$  at  $\alpha = 10$ . Considering  $E_0$  shown with the solid blue line in the lower panel, we see that  $E_0$  increases exponentially with  $\alpha$  with a value  $E_0 \approx 10^{-8}$  for  $\alpha = -10$  and  $E_0 \approx 10^0$  for  $\alpha = 10$ . We further see that the  $\alpha$  dependence of  $\gamma$  and  $E_0$  can respectively be modelled as

$$\gamma \approx 0.17\alpha + 1.1 \quad \text{and} \quad E_0 \approx 10^{0.4\alpha - 4}. \quad (8)$$

The lower panel also shows the mean FRB energy  $\bar{E}_{33}$  as a function of  $\alpha$  (dashed line). We have evaluated this by considering the entire FRB sample (both LELN and HEHN).

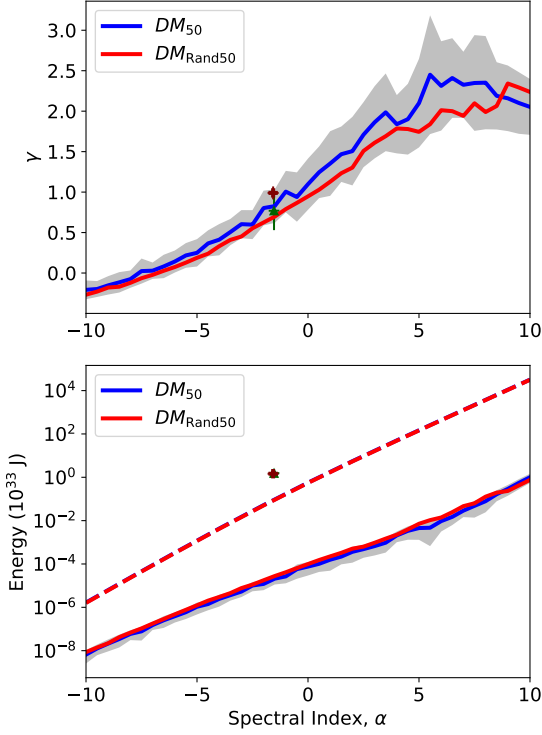


**Figure 5.** The variation of fitting parameters  $\gamma$  (upper panel) and  $E_0$  (lower panel) with the spectral index  $\alpha$ . The blue and red lines correspond to  $DM_{50}$  and  $DM_{\text{Rand}50}$  respectively. The dashed blue and red lines in the lower panel show the variation of the average energy  $\bar{E}_{33}$  with  $\alpha$  for  $DM_{50}$  and  $DM_{\text{Rand}50}$  respectively. The green triangle and brown plus symbols show the best fit parameter values ( $\alpha$ ,  $\gamma$ ,  $\bar{E}_{33}$ ) obtained from our previous analysis (Bhattacharyya et al. 2022) for  $DM_{50}$  and  $DM_{\text{Rand}50}$  respectively.

The entire analysis, until now, has assumed a fixed value  $DM_{\text{Host}} = 50 \text{ pc cm}^{-3}$  for all the FRBs. We next consider the situation where the  $DM_{\text{Host}}$  values have a random distribution. Here we have considered a situation where the  $DM_{\text{Host}}$  values are randomly drawn from a log-normal distribution with mean  $\mu = \log(50)$  and standard deviation  $\sigma = 0.5$ , and we refer to this as  $DM_{\text{Rand}50}$ . We note that the inferred  $z$  value depends on  $DM_{\text{Host}}$  (eq. 2), and for each FRB it is necessary to impose an upper limit on the randomly generated  $DM_{\text{Host}}$  in order to ensure that we can meaningfully estimate  $z$ . We have randomly generated 50 values of  $DM_{\text{Host}}$  for each FRB which leads to 50 energy tracks corresponding to each FRB. Considering the 254 FRBs in our sample, we have averaged 50 tracks for each FRB to estimate  $N(E_{33} | \alpha)$  for which the results are shown in Figure 6 for a few values of  $\alpha$ . We see that the results are quite similar to those shown in Figure 4 for  $DM_{50}$ , with the difference that there are no empty bins for  $DM_{\text{Rand}50}$ . Here also we see a difference between the FRB counts in the low and high energy ranges, although these differences are not as marked as they were for  $DM_{50}$ . For each  $\alpha$ , the  $E_{33}$  values used to demarcate the LELN and HEHN ranges for  $DM_{\text{Rand}50}$  were the same as those that we had used for  $DM_{50}$ . Considering the HEHN energy range, for each value of  $\alpha$  we have modelled  $n(E_{33} | \alpha)$  using a modified Schechter function. The best fit  $N(E_{33} | \alpha)$  (blue line) and the  $\chi^2_{\text{dof}}$  values are shown in the different panels of Figure 6. Here also, in all cases we find that the modified Schechter function provides a good fit to  $N(E_{33} | \alpha)$  in the HEHN regime. The  $\alpha$  dependence of  $\gamma$  and  $E_0$  for  $DM_{\text{Rand}50}$

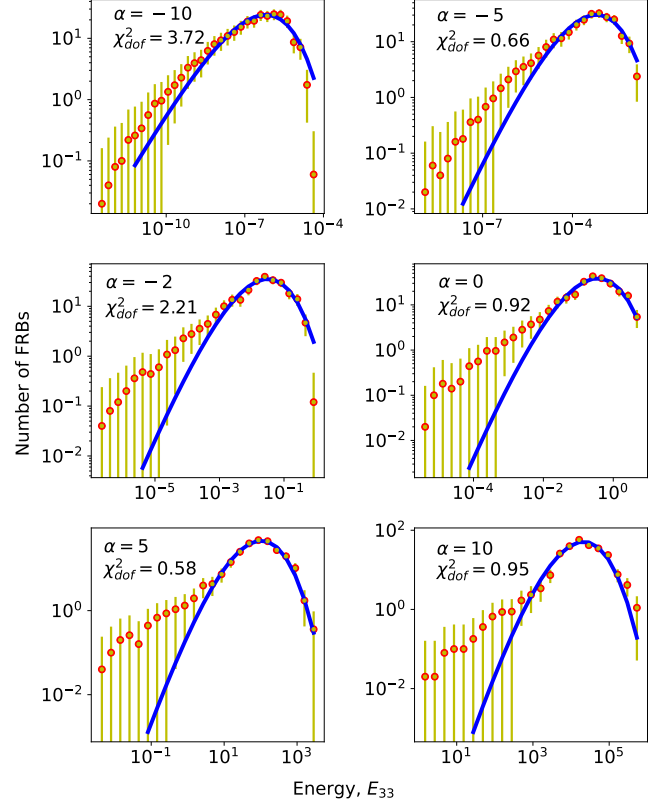


**Figure 6.** Same as Figure 4 for the  $DM_{\text{Rand}50}$

are also shown in Figure 5. We see that these are very similar to the results for  $DM_{50}$ , and we do not discuss them separately here.

In an earlier work (Bhattacharyya et al. 2022) we have used a sample of 82 non-repeating FRBs detected at Parkes, ASKAP, CHIME and UTMOST to obtain the best fit parameter values  $\alpha = -1.53^{+0.29}_{-0.19}$ ,  $\bar{E}_{33} = 1.55^{+0.26}_{-0.22}$  and  $\gamma = 0.77 \pm 0.24$ . For comparison, we have shown these best fit values along with the  $1\sigma$  error bars in Figure 5. Considering the upper panel, we see that the best fit values of ( $\alpha$ ,  $\gamma$ ) obtained in our earlier work are consistent with the results obtained in the present work. However, considering the lower panel, we see that the best fit values of ( $\alpha$ ,  $\bar{E}$ ) obtained in our earlier work are not consistent with the results obtained here. The present work does not jointly constrain ( $\alpha$ ,  $\bar{E}_{33}$ ,  $\gamma$ ), but instead it provides best fit values of ( $\bar{E}_{33}$ ,  $\gamma$ ) given the value of  $\alpha$ . Considering  $\alpha = -1.53$  which is the best fit value from our earlier work, the present analysis gives  $(\bar{E}_{33}, \gamma) = (0.173, 0.625)$  for which the value of  $\bar{E}_{33}$  falls below that obtained in our earlier work. However, it is necessary to note that a comparison is not straightforward as the approach used in the earlier work was quite different from that adopted here. The results from the earlier works depend on several input like (1.) the intrinsic FRB pulse width, (2.) the scattering model for pulse broadening in the IGM, and (3.) the  $z$  dependence of the FRB event rate, neither of which effect the present analysis. Further, the earlier work had a different model for  $DM_{\text{Host}}$ . All of these factors can effect parameter estimation and can possibly account for the difference in the values of  $\bar{E}_{33}$ .

The entire analysis, until now, has considered  $DM_{\text{Halo}} = 50 \text{ pc cm}^{-3}$  fixed, and two models for  $DM_{\text{Host}}$  namely  $DM_{50}$  and  $DM_{\text{Rand}50}$  both of which have a reference value of  $DM_{\text{Host}} =$

$50 \text{ pc cm}^{-3}$ . In order to check how sensitive our results are to these choices, we have redone the analysis considering other values of  $DM_{\text{Halo}}$  ( $= 40$  and  $60 \text{ pc cm}^{-3}$ ) and  $DM_{\text{Host}}$  ( $= 20, 40$  and  $60 \text{ pc cm}^{-3}$ ). The results are presented in Appendix A. We find that the main findings presented here are quite robust. The changes in the values of  $\gamma$  and  $E_0$  are found to be within 10% and 25% respectively.

#### 4 CONCLUSIONS

We have modelled the intrinsic properties of an FRB using its energy  $E_{33}$ , spectral index  $\alpha$  and redshift  $z$ . These completely determine the observed fluence  $F$  and extra-galactic dispersion measure  $DM_{\text{Ex}}$  provided other contributions to the  $DM$  are known. Here we have considered  $DM_{\text{Halo}} = 50 \text{ pc cm}^{-3}$  and  $DM_{\text{Host}} = 50 \text{ pc cm}^{-3}$ , and used the measured  $DM_{\text{Ex}}$  to infer  $z$ . The observed  $F$  then restricts the intrinsic properties of the particular FRB to a one-dimensional track in the two-dimensional  $\alpha - E_{33}$  parameter space. We refer to this as the energy track of the particular FRB.

Here we have used 254 energy tracks corresponding to a sample of FRBs detected at CHIME to determine  $N(E_{33} | \alpha)$  which is the number of FRBs in bins of equal logarithmic width  $\Delta(\log_{10}(E_{33})) = 0.2$ , given a fixed value of  $\alpha$ . Considering  $\alpha$  in the range  $-10 \leq \alpha \leq 10$ , we find that for all values of  $\alpha$  the measured  $N(E_{33} | \alpha)$  shows two distinctly different behaviour in different energy ranges. The estimated  $N(E_{33} | \alpha)$  has low values at low energies, and we refer to this as the LELN range. In contrast, at higher energies the estimated  $N(E_{33} | \alpha)$  increases with  $E_{33}$ , and rises to a peak value beyond which it declines. We refer to this as the HEHN range. In this paper we have modelled the FRB energy distribution in the HEHN range.

We find that in the HEHN range  $n(E_{33} | \alpha)$ , the conditional energy distribution, is well modelled by a modified Schechter function (eq. 7). The values of the fitting parameters  $\gamma$  and  $E_0$  are found to increase with  $\alpha$  (eq. 8). The present analysis, however, does not pick out a preferred value of  $\alpha$ .

We can use the  $n(E_{33} | \alpha)$  estimated in the HEHN range to predict the number of FRBs expected to be detected in the LELN range. We find that for all values of  $\alpha$  these predictions are much below the actual number of FRBs detected in the LELN range. This excess indicates that we are possibly seeing a different population of FRBs at low energies. However, the number of events is currently not large enough to study the FRBs energy distribution in the LELN range. We hope to address this in future when more FRB detections become available. Finally, we have checked that the findings presented in this paper do not change very much even if we consider different values of  $DM_{\text{Halo}}$  and  $DM_{\text{Host}}$ .

In future, we hope to carry out a combined analysis of the FRBs detected at different telescopes and use this to simultaneously constrain all three parameters ( $\alpha, E_0, \gamma$ ).

#### REFERENCES

Aghanim N., Akrami Y., et al., 2020, *A&A*, 641, A12  
 Amiri M., Andersen B. C., et al., 2021, arXiv preprint, 2106.04352  
 Bera A., Bhattacharyya S., et al., 2016, *MNRAS*, 457, 2530  
 Bhandari S., Sadler E. M., et al., 2020, *ApJ Letters*, 895, L37  
 Bhattacharyya S., Bharadwaj S., 2021, *MNRAS*, 502, 904  
 Bhattacharyya S., Tiwari H., et al., 2022, *MNRAS: Letters*, 513, L1  
 Caleb M., Spitler L. G., Stappers B. W., 2018, *Nature Astronomy*, 2, 839  
 Chawla P., Kaspi V. M., et al., 2022, *The Astrophysical Journal*, 927, 35  
 Cordes J. M., Lazio T. J. W., 2003, arXiv preprint, astro-ph/0207156

Cui X., Zhang C., et al., 2022, *Astrophysics and Space Science*, 367, 1  
 Gupta V., Bailes M., et al., 2020, *The Astronomer's Telegram*, 13788, 1  
 Houben L. J. M., Spitler L. G., et al., 2019, *A & A*, 623, A42  
 James C. W., Prochaska J. X., et al., 2021, arXiv preprint, 2101.08005  
 James C. W., Prochaska J. X., Macquart J. P., North-Hickey F. O., Bannister K. W., Dunning A., 2022, *MNRAS*, 509, 4775  
 Josephy A., Chawla P., et al., 2021, *The Astrophysical Journal*, 923, 2  
 Law C. J., et al., 2020, *The Astrophysical Journal*, 899, 161  
 Lorimer D. R., Bailes M., et al., 2007, *Science*, 318, 777  
 Lu W., Piro A. L., 2019, *ApJ*, 883, 40  
 Macquart J. P., Shannon R. M., et al., 2019, *ApJ Letters*, 872, L19  
 Marcote B., et al., 2020, *Nature*, 577, 190  
 Palaniswamy D., Li Y., Zhang B., 2018, *ApJ Letters*, 854, L12  
 Parent E., et al., 2020, *The Astrophysical Journal*, 904, 92  
 Pilia M., et al., 2020, *The Astrophysical Journal Letters*, 896, L40  
 Platts E., Weltman A., et al., 2019, *Physics Reports*, 821, 1  
 Pleunis Z., Good D. C., et al., 2021, *The Astrophysical Journal*, 923, 1  
 Price D. C., et al., 2018, *The Astronomer's Telegram*, 11376, 1  
 Prochaska J. X., Zheng Y., 2019, *MNRAS*, 485, 648  
 Rafiei-Ravandi M., et al., 2021, *The Astrophysical Journal*, 922, 42  
 Rajwade K. M., Bezuidenhout M. C., et al., 2022, arXiv preprint, 2205.14600  
 Ravi V., et al., 2019, *Nature*, 572, 352  
 Spitler L. G., Cordes J. M., et al., 2014, *ApJ*, 790, 101  
 Zhang B., 2020, *Nature*, 587, 45  
 Zhu W., et al., 2020, *The Astrophysical Journal Letters*, 895, L6  
 van Leeuwen J., Kooistra E., et al., 2022, arXiv preprint, 2205.12362

#### APPENDIX A: THE EFFECT OF VARYING $DM_{\text{HALO}}$ AND $DM_{\text{HOST}}$

Here we have studied the effect of varying  $DM_{\text{Halo}}$  and  $DM_{\text{Host}}$ . We first consider  $DM_{\text{Halo}} = 50 \text{ pc cm}^{-3}$  fixed, and vary the value of  $DM_{\text{Host}}$  to  $20 \text{ pc cm}^{-3}$  ( $DM_{20}$ ) and  $40 \text{ pc cm}^{-3}$  ( $DM_{40}$ ) for which the results are shown in Figure A1. It is not possible to consider a fixed  $DM_{\text{Host}} > 50 \text{ pc cm}^{-3}$  as this would exceed  $DM_{\text{Ex}}$  for some of the FRBs in our sample. We have next considered random  $DM_{\text{Host}}$  values drawn from log-normal distributions with  $(\mu, \sigma) = (\log(40), 0.4)$  and  $(\log(60), 0.6)$  for which the results are shown in Figure A2. Finally, we have varied  $DM_{\text{Halo}}$  to 40 and  $60 \text{ pc cm}^{-3}$  maintaining  $DM_{\text{Host}} = 50 \text{ pc cm}^{-3}$  fixed, for which the results are shown in Figure A3. In all of these figures panels (a) and (b) show  $N(E_{33} | \alpha)$  for  $\alpha = -5$ . These panels also show the predictions of the best fit modified Schechter function. In all of the cases considered here, we find that the modified Schechter function provides a good fit to the observed FRB energy distribution in the HEHN region. Panels (c) and (d) of all the figures show the fitting parameters  $\gamma$  and  $E_0$  for different values of  $\alpha$ . Considering  $DM_{50}$  (Figure 5) as the reference model, and comparing the results with those in Figure A1-A3 we find that the changes in the values of  $\gamma$  and  $E_0$  are within 10% and 25% respectively.

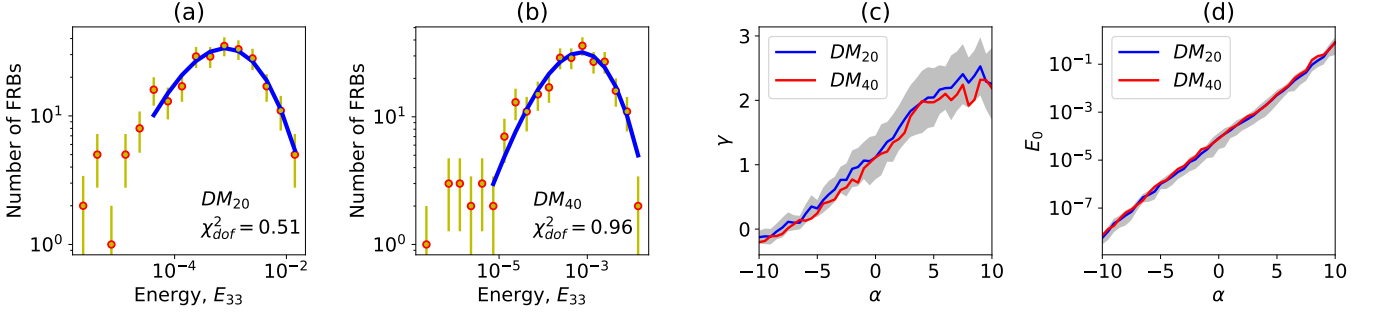


**Figure A1.** Results for two  $DM_{\text{Host}}$  models as indicated in the figure. Panels (a) and (b) show  $N(E_{33} | \alpha)$  (with  $1\sigma$  errors) as a function of  $E_{33}$  for  $\alpha = -5$ , while the solid line shows the predictions of the best fit modified Schechter function. The value of the reduced chi-square for the fit is indicated in the corresponding panels. Panels (c) and (d) respectively show the variation of the fitting parameters  $\gamma$  and  $E_0$  with  $\alpha$ .

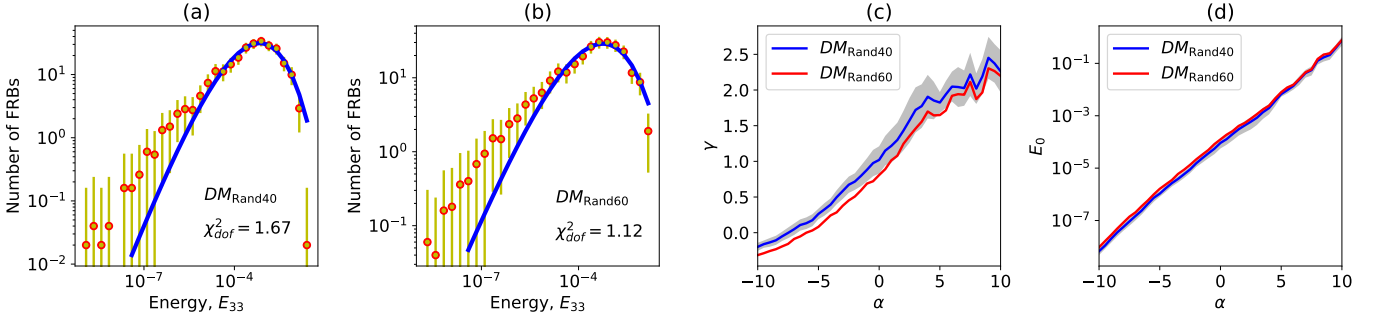


**Figure A2.** Same as Figure A1 but with two different  $DM_{\text{Host}}$  models as indicated in the figure.

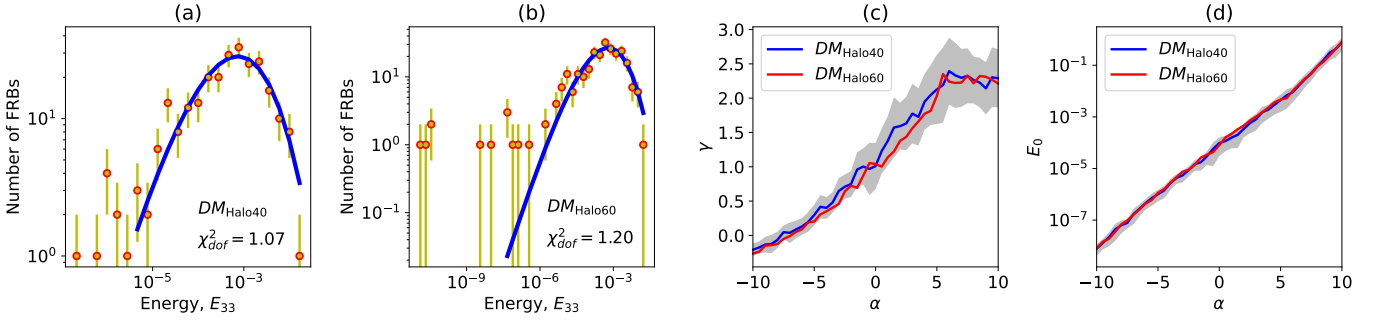


**Figure A3.** Same as Figure A1 but with two different  $DM_{\text{Halo}}$  models as indicated in the figure.